

# Femtosecond single- to few-electron point-projection microscopy for nanoscale dynamic imaging

A. R. Bainbridge,<sup>1,2</sup> C. W. Barlow-Myers,<sup>1</sup> and W. A. Bryan<sup>1, a)</sup>

<sup>1)</sup>*Department of Physics, College of Science, Swansea University, Singleton Park, Swansea, SA2 8PP, UK*

<sup>2)</sup>*Accelerator Science and Technology Centre, STFC Daresbury Laboratory, Daresbury Science and Innovation Centre, Keckwick Lane, Daresbury, Cheshire, WA4 4AD, UK*

(Dated: 8 December 2024)

Femtosecond electron microscopy produces real-space images of matter on micrometre to nanometre length scales in a series of ultrafast snapshots, tracking the dynamic evolution of charge distributions. Given that femtosecond pulses of electrons self-disperse under space-charge broadening, the ideal operation mode (without active compression) is a single electron per pulse. Here, we demonstrate for the first time femtosecond single-electron point projection microscopy (fs-ePPM) in a laser-pump fs-e-probe configuration. The electron pulses in the present work have an energy of only 150 eV and take tens of picoseconds to propagate to the object under study, striking a balance between keeping the distance between the fs-e source and object under study as small as possible and not exceeding the condition for DC field emission. Nonetheless, we achieve a temporal resolution with a standard deviation of 120 fs, combined with a spatial resolution below a micrometre. We image the evolution of a localized region of charge at the apex of a nanoscale metal tip induced by 30 fs 800 nm laser pulses at 50 kHz. The rapidity of the strong-field response of the metal nanotip facilitates the characterization of the number of electrons per pulse which is within limits established by an independent flux calibration. By comparing the spatial region of fastest experimental response to the outcome of charged particle modelling, we elucidate the electron pulse comprises on average one electron is not significantly influenced by space charge, rather geometric and kinematic broadening are the limiting factors. These observations demonstrate it is feasible to employ single-electron pulses for real-space imaging whilst maintaining femtosecond temporal resolutions. Dynamically imaging electric and magnetic fields and charge distributions on sub-micron length scales and sub-picosecond timescales opens up new avenues of ultrafast structural dynamics. Furthermore, through the use of active AC compression, such pulses are an ideal seed for few-femtosecond to attosecond imaging applications which will access sub-optical cycle processes in nanoplasmonics.

## I. INTRODUCTION

A wide variety of fundamental physical, chemical and biological processes occur on ultrafast timescales and atomic length scales. Direct visualization of such processes requires an imaging method with sufficient temporal and spatial resolution. The concept of pump-probe experiments serves extremely well in the temporal domain, whereby both the pump and probe pulses are engineered so as to have durations shorter than the characteristic timescale of the process under study. Fundamental processes such as charge migration, chemical dynamics or phase change phenomena require picosecond or better still femtosecond duration pulses, thus modern ultrafast laser technology, which operates on this timescale in the visible to infrared is very well suited. Clearly there is a disparity between atomic length scales and the wavelength of such laser sources, hence to access the few nanometre to tens of picometre length-scale, current ultrafast imaging paradigms have turned to very short wavelength (x-ray) photons or electrons. Advances in technology such as pulsed synchrotron sources and to a greater extent femtosecond X-ray Free Electron Lasers (X-FELs)<sup>1</sup> enable x-ray crystallography, microscopy and diffraction techniques in the femtosecond temporal regime[refs]. By stimulating the target with a laser pulse to cause a phase change, trigger phonons or induce charge density waves at a known delay before the arrival of the probing x-rays, a series of snapshots may be obtained showing the evolution of the system in both space and time with atomic spatial and temporal resolution.

Pushing the wavelength of photons ever shorter is a limitation that has been encountered in the 1930's, with a paradigm shift induced by the work of Knoll and Ruska at the University of Berlin in 1931, resulting in the Nobel Prize in Physics in 1986<sup>2</sup>. Electrons have a de Broglie wavelength three orders of magnitude smaller than a photon of equivalent energy, the realization of which led to the development of transmission electron microscopy. Producing electrons with energies from hundreds of eV to tens of keV is, as compared to XFELs, relatively straightforward.

<sup>a)</sup>Electronic mail: w.a.bryan@swansea.ac.uk

Combining femtosecond laser technology with electron sources, as first demonstrated in the early 1990's by Miller and co-workers<sup>3</sup> and Zewail and co-workers<sup>4</sup>, introduced a novel approach to ultrafast atomic scale imaging. Delivering electron bunches of nanometre to picometre wavelengths in pulses femtoseconds to attoseconds in duration is evolving from these initial experiments to create the potential for unprecedented insights into fundamental processes that continues to influence many research themes<sup>5-13</sup>.

Two fundamental emission processes have been demonstrated to produce femtosecond pulses of electrons making use either of the energy of one or more photons<sup>141516</sup>, or the resulting electric field induced by a flux of photons<sup>1718</sup>. Illuminating a generally planar photocathode with a laser pulse with a photon energy that exceeds the work-function produces continuum electrons. The most common configuration is UV pulses and gold, however semiconductor emitters are also employed as they can operate in the infrared, generally the fundamental wavelength range of femtosecond lasers. A disadvantage of using such emission processes is that the emission site is limited by the size of the laser focal spot, typically tens of microns, reducing the transverse coherence. It has been demonstrated that illuminating a cloud of ultracold atoms with a photon energy just above the work function results in low temperature electrons of high coherence, albeit at long pulse durations.

The emission process used in the present work is inspired by the work of Ropers<sup>1419</sup>, Hommelhoff<sup>20212223</sup>, Ernstorfer<sup>2425</sup> and Baum<sup>26,27</sup>. A Nanoscale Metal Tip (NSMT) is a cylindrically symmetric wire that tapers to an apex of tens of nanometres in diameter, hence conceptually identical to field emitters employed in TEM. Rather than rely on a photon to exceed the work function of material, the small radius of curvature at the NSMT apex causes a significant field enhancement when an electric field gradient is applied to the NSMT. DC field emission has been employed to demonstrate point-projection microscopy and requires only the application of a voltage, and the resulting electric field gradient at the apex is sufficient to allow electrons near the Fermi level to tunnel directly into the continuum<sup>28,29</sup>. Applying a femtosecond laser pulse of moderate intensity causes the same process<sup>15</sup> in what is referred to as the strong-field regime. The barrier to the continuum can only be tunnelled during the laser pulse, therefore the emitted electron pulse duration can be tens of femtoseconds.

The realization of this time-varying field-enhancement in conductors such as tungsten, gold and silver (which are readily electrochemically etched to nanometre points) and semiconductor nanospheres  $\text{SiO}_2$  (which can be monodispersed down to tens of nanometres) has initiated the highly active research field of ultrafast nanophotonics or femtosecond nanophysics. Themes including optical near-field sensing, sub-cycle carrier-envelope phase phenomena, investigations into surface plasmons and laser-driven electron accelerators have emerged<sup>30-33</sup>. The present work aligns itself to these efforts by looking to better quantify the spatial and temporal characteristics of femtosecond laser-driven electron microscopy.

Femtosecond electron emission, be it from a planar photocathode or NSMT, generally results in a kinetic energy below 5 eV and a bandwidth defined by the laser pulse spectrum<sup>34151923</sup>. Acceleration is necessary to reduce the de Broglie wavelength and minimize the kinematic dispersion due to variations in particle velocity. Furthermore, if there is more than one electron per pulse, the electron-electron repulsion results in a spatial dispersion therefore temporal stretching, referred to as space-charge broadening<sup>3536</sup>. Both kinematic dispersion and space-charge broadening are minimized by transporting the electron pulse to the target under study as quickly as possible<sup>37</sup>. DC electrostatic acceleration is limited by vacuum breakdown, imposing a minimum flight path between the electron source and target, and the difficulties associated with transmission of a voltage above around 300 kV into vacuum serves as an upper limit. Radio-frequency AC fields facilitate acceleration to relativistic electron energies, and can also be used to form a temporal lens by applying a spatial chirp to the electron velocity. This technique has been demonstrated by Luiten and co-workers, achieving a standard deviation (SD) pulse duration of 80 fs<sup>3839</sup>. More recently, Baum and co-workers have compressed single electron pulses to 28 fs FWHM with a microwave field addressing compression rather than high charge density<sup>40</sup>.

In this work, we look to push the performance of the most simple real-space ultrafast electron imaging method to its temporal limits. Femtosecond electron point-projection microscopy (fs-ePPM) has been demonstrated previously by Ropers<sup>9</sup>, Ernstorfer<sup>2425</sup> and Barwick<sup>41</sup>. In these publications, the intention was to study fundamental processes, whereby the phenomenon under study was well suited to the temporal resolution. These studies were highly successful, and demonstrate the potential for fs-ePPM, which has significant advantages over more complex higher energy configurations. Taking a point source, here a NSMT, and allowing femtosecond pulses of electrons to diverge electrostatically results in lensless magnification if the sample or target under study is placed a short distance from the electron source. After passing the target, the transmission modified electron pulse is recorded a large distance from the source, and the source-detector to source-target ratio is then the magnification. In fs-ePPM, magnifications of 5000 have been achieved<sup>41</sup>. This is compared to the work of Fink and co-workers with DC field emission PPM<sup>2829</sup>, who have achieved magnifications of in excess of  $10^4$  [check this source]. The requirement for keeping the electron flight path short while maximizing the energy is the cause of this difference.

Looking to generate and characterise short electron pulses requires we operate with as few electrons per pulse as possible, thereby requiring a process that can be cycled repeatedly, preferably at high laser repetition rates.

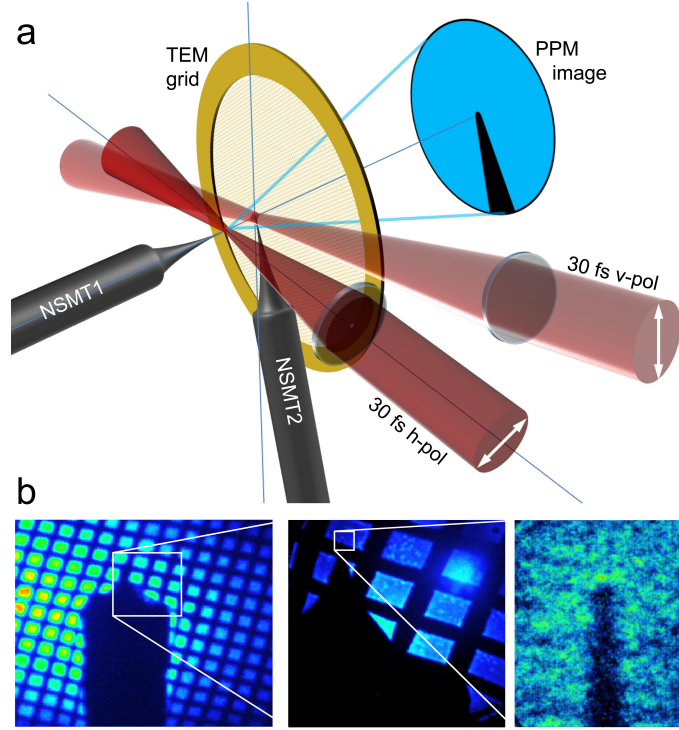


FIG. 1. (a) Schematic of the femtosecond electron point-projection microscope demonstrated. A nanoscale metal tip (NSMT1) was illuminated with horizontally polarized  $\lambda = 800$  nm 30 fs duration laser pulses at a repetition rate of 50 kHz. The apex of NSMT1 had a radius of curvature of approximately 50 nm and the laser pulses were transmission focused to a spot size of  $5.4 \mu\text{m}$ . A pulse energy of 45 nJ produced a peak intensity of  $1.2 \times 10^{12} \text{ Wcm}^{-2}$  however the apex of NSMT1 experienced less than 1/20th the intensity. NSMT1 was held at a potential of -150 V with respect to a grounded TEM grid, accelerating the resultant femtosecond electron (fs-e) pulses towards a distant microchannel plate detector, forming a point-projection image. Nanoscale metal tip 2 (NSMT2) was illuminated by vertically polarized laser pulses from the same source and a comparable intensity. A significantly longer focusing optic ( $f = 300$  mm as compared to  $f = 75$  mm) illuminates a region above the apex of NSMT2, resulting in a localized time-varying charge distribution. (b) Low magnification to high magnification PPM images of NSMT2 using electrons emitted from NSMT1. Each image is the sum of  $5 \times 10^5$  laser shots. For scale, the NSMT diameter below the taper is 0.25 mm, and the square holes visible in the TEM grid are 60 microns square.

Furthermore, we require a target which can be pumped with an infrared laser pulse (i.e. not requiring conversion to the UV or higher photon energies) and which reacts by causing a highly localized emission of charge, creating a measurable distortion to our femtosecond electron (fs-e) pulse. We therefore select a second NSMT as the target.

As discussed, the transfer of bound electrons to the continuum is constrained by the duration of the laser pulse. Our previous work<sup>34</sup> allows us to operate entirely in the strong-field regime, where emission of electrons on either NSMT is due to the local field enhancement, rather than the transfer of significant energy to either NSMT causing thermionic emission. Achievement of femtosecond temporal resolution requires the issue of pulse broadening to be addressed, which is achieved in this work on two fronts. Space charge broadening is countered by generating an average of a few electrons per laser shot, and producing an image at each delay by integrating over  $5 \times 10^5$  laser shots at a repetition rate of 50 kHz. Broadening due to the natural bandwidth of the electrons is minimized by keeping a compact geometry where electrons are able to rapidly traverse the distance to the sample despite their low energy, a convenient arrangement which improves both the temporal resolution and magnification of point-projection microscopy

## II. EXPERIMENTAL

An electron point-projection microscope was constructed using two electrochemically etched tungsten NSMTs, fabricated from polycrystalline tungsten wire of diameter 0.25 mm. Apexes of tens to hundreds of nanometres are routinely produced using standard methods [REF]. An illustration of the experimental configuration is presented in figure 1(a). A source tungsten NSMT (referred to as NSMT1 throughout) with independently controllable applied

voltage acted as a photocathode and was positioned on a vibration-isolating mount located concentrically with a grounded TEM grid. The distance between the nanotip and the grid was adjustable via an external translation stage from contact to a separation of approximately 1 cm, with 1 micron precision. The TEM grid was in turn supported by a vibration isolating and electrically insulating mount, and was concentric to a position sensitive electron detector a distance of 0.44 m further down the electron flight path. The detector consists of a pair of micro-channel plates (Burle) and a P22 phosphor screen (Kimball Physics), referred to as MCP+PS, and was imaged by a CCD camera (Pike-145B, Allied Vision Technologies). A second tungsten nanotip (referred to as NSMT2) was used as the sample and was placed between the source tip and the TEM grid, attached to the grid mount but with an independently controllable voltage via a 25  $\mu\text{m}$  diameter gold wire connected beyond the outer edge of the TEM grid. Independent control of the potential applied to NSMT2 and the TEM grid gave control over the electrostatic lensing of the probe electrons.

The apparatus illustrated in figure 1(a) was contained in an ultra-high vacuum chamber with a base pressure of  $3 \times 10^{-9}$  mbar. The chamber was configured such that both the tip and sample are secured directly to the optical table and connected to the rest of the chamber only via flexible bellows, ensuring that they were isolated from the vibration and, should they be caused to vibrate, that they do so together. A mu-metal shield surrounding the volume between the TEM grid and the detector prevented the electron flight from being disrupted by magnetic fields, and a 3-axis Helmholtz coil arrangement was used to neutralize magnetic fields in the interaction region and to provide beam steering at low magnifications.

Femtosecond laser pulses were produced by a Yb:KGW regenerative amplifier (Pharos, Light Conversion) operating at a repetition rate of 50 kHz, which pumped a Non-collinear Optical Parametric Amplifier (NOPA) (Orpheus-N, Light Conversion) operating at a centre wavelength of 800 nm. The NOPA generated sufficient bandwidth to give a transform-limited duration of 14 fs. The NOPA output was compressed to sub-30 fs in a prism compressor which pre-compressed the dispersion introduced by material outside the vacuum, specifically a 3.3 mm thick fused silica window and a 2.4 mm thick UV fused silica lens. The duration of the pulse following transmission through this material was confirmed as 28 fs using Frequency-Resolved Optical Gating (FROG), used to provide shot-to-shot monitoring of the pulse length and bandwidth.

The NOPA output was split and each arm directed through separate periscopes configured to ensure that the light arriving at NSMT1 and NSMT2 was polarized along the tip axes. As the strong-field ejection of electrons from NSMTs has been demonstrated to be polarization dependent<sup>42,43</sup>, illuminating with crossed polarizations ensured NSMT1 would not emit even if a small part of the NSMT2 laser focus overlapped and vice versa. The pulse to NSMT2 also passed through a delay stage capable of introducing 500 ps of additional flight time with 6.7 fs precision.

Low, medium and high magnification fs-ePPM images are shown in figure 1(b), indicating how NSMT2 is located. Manipulating the magnification requires the distance between NSMT1 and NSMT2 to be varied, hence the position of the focus of the horizontally polarized laser pulse must move with NSMT1. This fine control was achieved by making small adjustments to the position of the focusing optic with differential micrometers.

### III. MODELLING

To quantify the performance of our fs-ePPM system, we established a numerical model in two stages. The Superfish Poisson equation solver (LANL) was used to model the electrostatic field between NSMT1 and the plane of the TEM grid. The shape of a series of NSMTs was recorded using an optical microscope, as shown in figure 2(a). A strong backlight was employed to give crisp image contrast. Clearly, optical methods cannot resolve the apex of a NSMT, however they allow a typical shape of the tapering region to be determined. The result of these measurements are shown in 2(b), where an edge detection method was used to find a line that characterized the shank of the NSMTs. Average tip and shank angles were found to be 17 and 55 degrees. We approximated this combined profile with ten straight sections from the cylindrical edge of the tungsten wire, followed by a 20  $\mu\text{m}$  section at the tip angle. The apex of the NSMT model was treated as a 50 nm diameter sphere meeting this straight section at a tangent.

With NSMT1 450  $\mu\text{m}$  from the TEM grid, Superfish produced the representative electric field map shown in figure 2(c). With the correct potentials applied to each solid object (NSMT1 at -150V, TEM grid at 0 V), the code employs the successive over-relaxation method to calculate the magnitude and direction of the electric field at each mesh vertex. The influence of the small radius of curvature of the apex is apparent from the bunching of field equipotential near zero. As the Poisson solver operates on a regular mesh, it was necessary to change the mesh spacing in the vicinity of the apex, as shown in figure 2(d). We observed the recommended minimum grid spacing variations to allow Superfish to manage an apex of tens of nanometres on an object of hundreds of microns in diameter. The mesh spacing was optimized such that the field lines showed no discontinuities.

The electrostatic field was then interpolated and imported into the General Particle Tracer (GPT, Pulsar Physics) charged particle tracking code. The sample tip is omitted from the calculation as it is known from the experimental

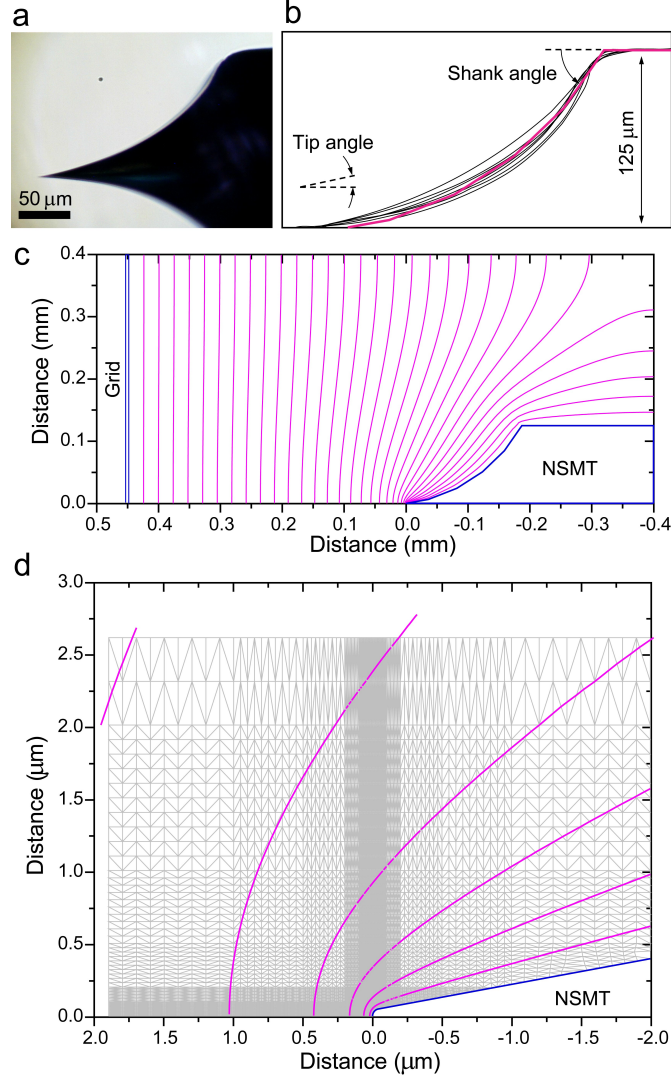


FIG. 2. (a) Optical microscope image of a typical NSMT. (b) By thresholding and edge detecting images such as (a), we find a series of lines that represent the typical shape of our tungsten NSMTs (black lines). The magenta line is the approximation to this shape used in the Superfish Poisson solver. (c) Superfish output of PPM geometry with the TEM grid at 0 V and the NSMT at -150 V. (d) Superfish field map at NSMT1, showing changing mesh size to accommodate millimetre flight length and nanometric tip apex.

results that it is possible to hold the sample at a voltage which approximates electrically floating, as evidenced by the absence of a lensing effect. This is also necessary to allow the codes to approximate a rotationally symmetric system to dramatically reduce computational requirements. As the number of electrons per pulse was unknown, our simulations of their propagation from NSMT1 to the TEM grid requires the inclusion of space charge. GPT decouples the charge per pulse from number of simulation elements by defining identical macro-particles, here 50,000. The total charge of these macro-particles is then defined and can be varied arbitrarily. GPT solves Poisson's equation in three dimensions in the rest frame of the electron pulse for all macro-particles. This is treated using a particle-in-cell method rather than calculating all pair-wise interactions.

The dynamic propagation of the fs-e pulse is modelled in GPT by assuming an emission energy of 4.5 eV and a bandwidth of 0.3 eV, in agreement with recent studies<sup>20,23,34</sup>. The point of origin of the electrons was defined to lie along the surface of the apex of NSMT1, and the emission time defined as a Gaussian distribution with a SD of 30 fs. GPT calculates the trajectory of the electrons with a 5th-order Runge-Kutta algorithm with variable step size defined by an accuracy of  $1:10^{-6}$ .

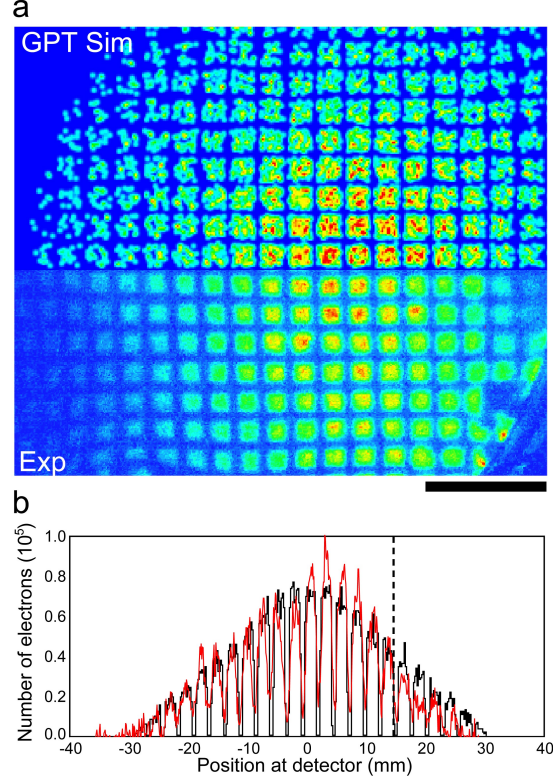


FIG. 3. (a) Comparison of output of the GPT model (top) with experimental observations (bottom) of electron propagation from NSMT1, through a TEM grid at 2.45 mm from NSMT1, then on through a field free region to the MCP detector 0.44 m distant. This agreement allows independent conformation of magnification and source size. The scale bar is  $350 \mu\text{m}$  at the TEM grid. (b) A direct comparison of the predicted and observed electron distribution following low magnification fs-ePPM. The agreement to the left of the dashed line is compromised by edge effects in the detector.

#### IV. PPM MAGNIFICATION AND SOURCE SIZE

The first quantification of the fs-e pulse emission was the diameter of the electron emission site. With NSMT2 lowered out of the electron path, a fs-ePPM image of the TEM grid was recorded as presented in figure 3(a). The magnification was intentionally set low so as to illuminate many grid squares. The TEM grid was 300 mesh square copper, with a bar width of  $25 \mu\text{m}$  and a centre to centre spacing of  $85 \mu\text{m}$ . The GPT code was modified to include an analogous pattern of electron absorbing elements, representing the TEM grid. After propagating from NSMT1 to the TEM grid, the electron pulse then flies field-free to the plane of the detector 0.44 m distant and the distribution of arrival positions recorded.

The spatial distribution of the initial electron position on the apex of NSMT1 was Gaussian, centred on-axis with a standard deviation (SD) defined as a ratio of the NSMT1 apex radius, initially set to 1 hence all of the spherical apex was treated as emitting. The NSMT1-TEM grid distance was varied in the simulation until the magnification of the TEM grid period matched that observed on the MCP+PS detector. The NSMT1 to TEM grid distance retrieved using this method was  $2.45 \pm 0.02 \text{ mm}$ , with the estimate of uncertainty the minimum resolvable discrepancy between model and measurement. All subsequent translations of NSMT1 were made with respect to this point.

The spatial distribution of electron origin was then varied to best reproduce the experimental observations. Decreasing the SD of the Gaussian emission distribution from the NSMT1 apex (i.e  $50 \text{ nm}$ ) in  $5 \text{ nm}$  steps, it was found that the best reproduction of the observations was found with an emission site of radius  $10 \text{ nm}$ . This is shown in figure 3(a) and a section through the middle of the observed distribution overlapped directly with the model result is shown in figure 3(b). A variation of  $3 \text{ nm}$  is the lower limit of observable deterioration in this agreement.

## V. ELECTRON FLUX CALIBRATION

Quantifying and minimizing space charge broadening is a key aim of this work, hence an independent calibration of the fs-e flux is required. If the quantum efficiency of the microchannel plates, phosphor screen, vacuum window, imaging lens and camera were well known, direct calibration would in principle be possible. This was hampered by both the MCP and PS performance varying as a function of time, hence such a recalibration would need to be performed regularly. Furthermore, an emitter producing a well-characterized flux of electron would be needed.

We turned therefore to the UHV and imaging capabilities of our electron detector. The typical operating pressure of this instrument was  $6 \times 10^{-9}$  mbar, hence the detector was intrinsically low noise. Typically, the full active areas of the MCP+PS registered less than one background count per second with the fs-e source off. Under typical operating conditions, the front of the MCP pair was negatively biased by between 10 and 20 V to prevent stray electrons from our full-range pressure gauge (HPT 100, Pfeiffer Vacuum) being collected while still allowing fs-ePPM electrons to pass.

Before recording fs-ePPM images we performed a simple calibration measurement: with NSMT1 not emitting but the MCP+PS set to operational conditions, we varied the voltage on the front of the MCP until the detector was collecting tens of gauge electrons per exposure (286 ms). Then, by manually counting the number of electrons per exposure, we have a route to converting signal at the AVT Pike to electrons arriving at the front of the MCP. The variation of MCP efficiency with electron energy is known (80 at 300 eV to 50 at tens of eV), hence a count rate conversion was applied between gauge electrons and laser-generated fs-electrons. This process was repeated for a range of detector conditions and was found to be reproducible day-to-day on the condition that the laser illumination of NSMT1 was held as constant as possible. This was made possible by imaging the NSMT1 laser drive pulse on exit of the vacuum chamber: the laser pulse passing NSMT1 induces a weak diffraction effect, recorded with an IR-sensitive webcam.

## VI. RESULTS - FEMTOSECOND ELECTRON MICROSCOPY OF A NANOSCALE METAL TIP

The separation between NSMT1 and NSMT2 was reduced to hundreds of microns. With no laser illumination on NSMT2, NSMT1 was translated from the calibrated magnification position producing a series of images as shown in figure 1(b). Typical magnifications were in excess of  $10^3$ , which should elucidate the smallest features on the apex of NSMT2, however are not sufficient to facilitate the observation of in-line holograms.

With NSMT1 laser illuminated and generating fs-e pulses, NSMT2 was laser illuminated and the delay between the arrival time of the fs-e pulse and the vertically polarized laser pulse at NSMT2 scanned. The NSMT1 to NSMT2 flight time prediction from the GPT model allowed constraints to be placed on the delay range. Furthermore two fast photodiodes (DET-10A, Thorlabs) recorded the laser pulses on the exit of the vacuum chamber giving an absolute measurement of the laser pulse arrival times, albeit at a resolution 5 orders of magnitude lower than the laser pulse durations.

As shown in figure 4(a), as the delay between the horizontal and vertical polarized laser pulses is scanned over 8 picoseconds, the image of the apex of NSMT2 appears to expand. This is followed by the shank of NSMT2 blurring at longer delays. Such exposures are recorded with  $5 \times 10^5$  laser pulses, therefore the temporal evolution of the image of NSMT2 is repeatable and not the result of the vertically polarized laser pulse destroying the end of NSMT2. Rather, laser illumination of NSMT2 causes low energy electron ejection from the apex just as with NSMT1. As this charge distribution is not strongly accelerated, it remains in the vicinity of NSMT2 and the trajectory of the passing fs-e pulse is distorted by electron-electron repulsion.

The expansion and propagation of the dark region with time indicates regions of high charge density on the surface of the nanotip triggered by the laser pulse. These regions deflect passing electrons in the probe pulse expanding the shadow of the tip around the highest charge density regions.

Figure 4(a) reveals that the charge propagation appears to occur in stages. Between temporal overlap and approximately 1.3 ps there is a strong but localized increase in charge density concentrated at the very end of the tip, which for positions close to the apex has a rise time of approximately 1.5 ps. Between 1.3 and 2.3 ps this charge cloud begins to expand away from the apex, before finally, between 2.3 and 3.3 ps, the charge cloud begins to propagate down the taper of the tip. This occurs preferentially on the side of the tip from which the laser is incident.

The spacing of the images in figure 4(a) is two picoseconds hence the duration of the fs-e pulse must be shorter than this step size. We better elucidate the temporal behaviour by presenting horizontal (figure 4(b)) and vertical (figure 4(c)) sections through the time-varying image of NSMT2, at the positions indicated by the white lines in figure 4(a). These are shown in the right-hand panels of figure 4(b) and (c). In figure 4(b), the lower part of the left-hand most image in figure 4(a) is presented for spatial reference. To allow direct comparisons between the horizontal and vertical sections, the left-hand panel in figure 4(b) is rotated clockwise 90 degrees.



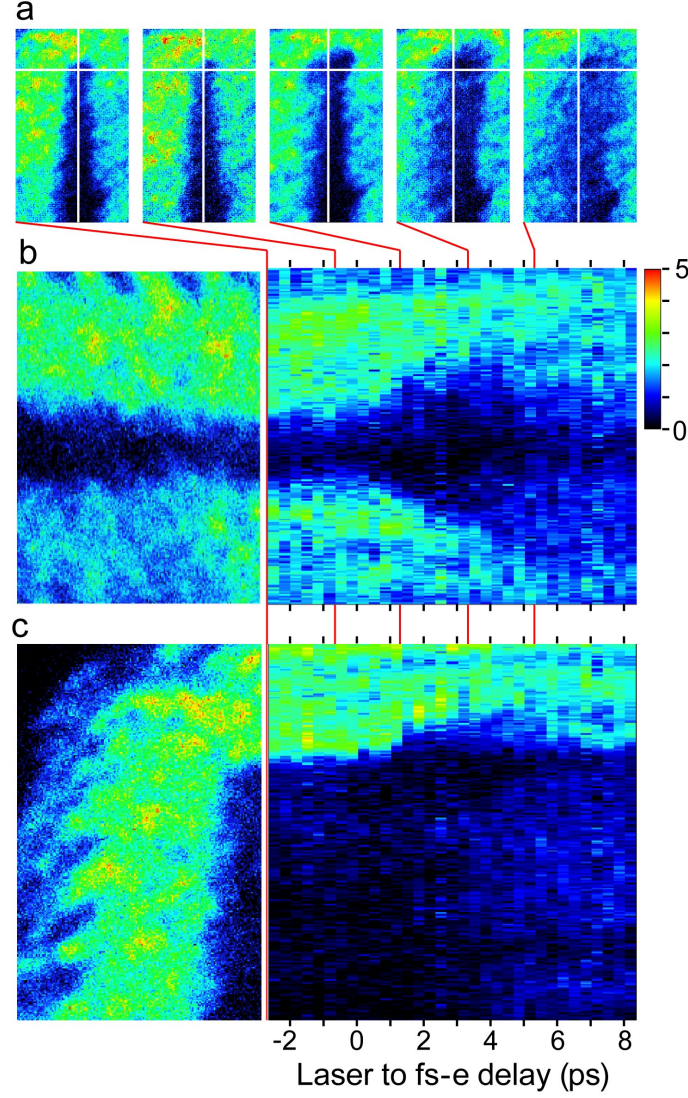


FIG. 4. Femtosecond electron point-projection microscopy of nanoscale metal tip 2 (NSMT2) illuminated with an infrared 30 fs laser pulse. (a) Sequence of PPM images of NSMT2. Presented are (left to right) -2.66 ps, -0.67 ps, 1.33 ps, 3.33 ps and 5.33 ps where time zero is the point at which the fs-e and laser pulses arrive at NSMT2 simultaneously. Horizontal and vertical lines indicate positions of (b) and (c) which are time-dependent slices through the dataset. (b) (left) Part of the -2.67 ps spatial image below the white line, rotated clockwise by 90 degrees. (right) Sections through the time-dependent image dataset along the horizontal line in (a) as a function of laser-fs-e delay. Each slice is 9 pixels wide, corresponding to 50 nm. The flare at positive delay is due to electron-electron scattering from apex of NSMT2 induced by strong-field electron ejection. (c) (left) As (b) but for the left-hand part of the -2.67 ps image, followed by (right) the temporal evolution of 9 pixel wide slice as function of laser-fs-e delay.

As the delay between the arrival of the laser and fs-e pulses at NSMT2 switches from fs-e then laser (negative delay) to laser then fs-e (positive delay), the time-dependent expansion of the apex of NSMT2 can be observed, the result of the onset of laser-induced charging, which then dissipates down the shank of NSMT2 over hundreds of picoseconds. The mechanics behind this process will be the subject of future work. Here, we only assume that the charging process can be as short in time as the laser pulse duration.

It is interesting to note that the charge expansion observed at NSMT2 does not have reflection symmetry. In figures 4(a) and (c), the laser pulse arrives from the left, while in 4(b) it arrives from the top. It is suggested that the asymmetry of emission is then due to diffraction of the vertically polarized laser pulse by NSMT2, thus modifying the emission site shape.



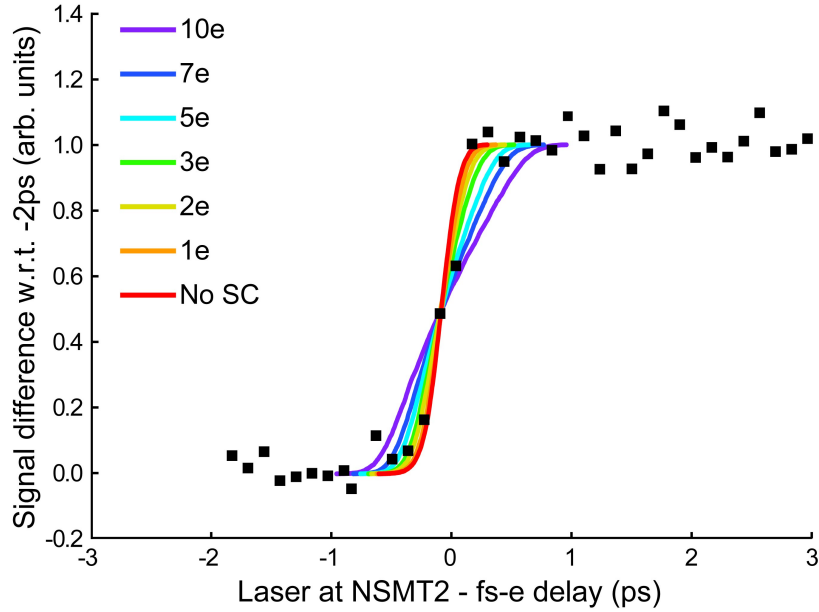


FIG. 5. Comparison between the measured difference between large negative laser-fs-e pulse delay and subsequent fs-ePPM images (black squares), and the predicted cumulative electron flux at the plane of NSMT2 (coloured lines) as the average number of electrons per pulse is varied between zero electrons (No SC) and 10 electrons. The laser-induced charging of NSMT2 switches on rapidly but dissipates slowly, hence using the cumulative signal difference. The signal is found by taking a  $9 \times 9$  square of pixels on subsequent images and taking the difference between the comparable point on the -2 ps dataset. The comparison of these measurements to the GPT predictions allows the number of electrons per pulse to be inferred.

## VII. RESULTS - NUMBER OF ELECTRONS PER FEMTOSECOND ELECTRON PULSE

The data presented in figure 4 contains a significant amount of information about the laser-induced process around NSMT2, however here we limit ourselves to looking for the fastest possible behaviour. The rationale behind this is that a process developing over a characteristic timescale shorter than the duration of the fs-e pulse can give metrological insight. Furthermore, other fs-e characterisations cannot be employed in the current configuration. Looking for thermionic charging of the TEM grid as employed by<sup>9</sup> is limited to picoseconds. Ponderomotive electron scattering from counter-propagating laser pulses<sup>44</sup> requires pulse energies orders of magnitude higher than the NOPA is capable of generating. Electron streaking is too slow. RF cavity deflection is not possible with the current configuration and is limited in terms of synchronization. The nonlinear response of NSMT2 to 30 fs laser illumination is therefore a good compromise: it is highly localized, of a comparable duration and is very well synchronized.

With this in mind we find the spatial region exhibiting the most rapid response as a function of the laser-fs-e delay. This is anticipated to be in the vicinity of the apex of NSMT2 where the field enhancement effect is strongest therefore resulting in the highest instantaneous change in charge. In figure 5 we such a condition using the difference in electron flux recorded as a function of laser-fs-e delay. The largest negative delay is taken as a zero point, and subsequent fs-e images of NSMT2 sequentially subtracted. We then take a  $9 \times 9$  pixel region around the point of fastest response. This size region is the best compromise between statistical stability and averaging out the temporal behaviour.

In figure 5 a rise-time well below 1 ps is observed. Quantification of the electron flux using the method described above indicated between 0.8 and 12 electrons per pulse arrived at the detector. While this estimate is informative, it has a large uncertainty, and we use the outcome of the numerical modelling of the fs-e propagation to demonstrate a significant improvement in quantifying how low flux pulses can be characterized as a function of time. As discussed earlier, single electron pulses overcome space charge broadening however are inherently poorly suited to ponderomotive, RF or thermionic methods.

GPT was employed to predict the distribution of macro-particle arrival times at the plane of NSMT2. The time of release from the apex of NSMT1 is a Gaussian distribution with a SD of 30 fs, however as this surface is spherical, the flight time to the plane of NSMT2 is influence by the trajectory taken. As a result of this and the finite bandwidth of the fs-e pulse, a duration somewhat larger than 30 fs is anticipated.

The laser-initiated field enhancement at NSMT2 switches on rapidly, then takes picoseconds to redistribute and for the apex to neutralize. Direct comparison of the measured rise-time with the number of macro-particles arriving at a

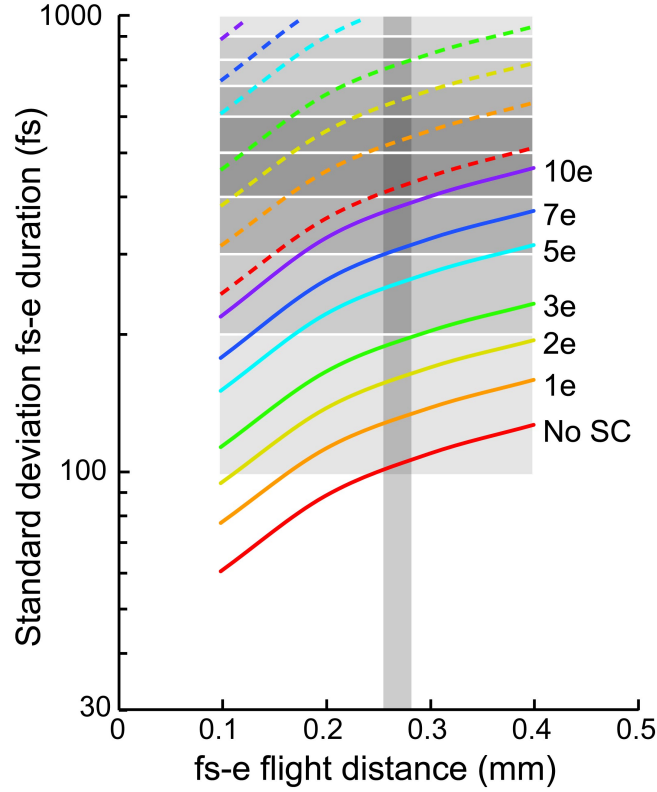


FIG. 6. Femtosecond electron pulse stretching on propagation from NSMT1 including space charge, geometric effects and energy bandwidth. The solid lines are the predicted standard deviation of the fs-e pulse width as a function of time at different points along the flight path between NSMT1 and NSMT2. The SD duration of the space-charge free fs-e pulse increases along the flight path, a result of the geometric stretch and energy bandwidth. The contribution of space charge can also be observed as the average amount of total charge in the pulse is increased from no space charge (No SC) to 10 electrons per pulse. The dashed lines are the  $2\sigma$  width of the corresponding Gaussian distribution, i.e.  $4 \times \text{SD}$ . Experimental constraints are indicated by the grey regions. The vertical thin grey box indicates the position of NSMT2 with respect to NSMT1, and the horizontal grey boxes indicate an estimate of the rise time of the signal. The grey-level varies linearly with gradient of the signal, seen to be a maximum between 400 and 600 fs. The overlap between these regions and the dashed lines facilitates an estimate of the electron flux, which is most likely to be between less than one electron to two electrons per pulse.

specific time is therefore meaningless, rather we take the cumulative number of particles as it better represents how the fs-e pulse is distorted. The outcome of these calculations is shown in figure 5 where the total charge of the fs-e pulse is varied between zero and ten electrons. With zero total charge, GPT still treats the pulse electrostatically but there is no space charge broadening. As the total charge in the pulse increases, a temporal broadening is predicted which is asymmetric around the temporal centre of the pulse.

Comparing the modelled and measured rise-times in figure 5, it is apparent our fs-e pulse on average comprises fewer than ten electrons. Indeed, looking at the agreement between the data around the largest gradient as a function of time, we argue that an average charge per pulse between one and three electrons is the best fit to the experimental data.

This is highlighted in figure 6 where we show the SD fs-e duration as a function of propagation distance. These predictions indicate how space charge broadening influences the pulse as it flies. Should it be possible to separate NSMT1 and NSMT2 by  $100 \mu\text{m}$  or less, electron pulses well below 100 fs could be delivered to target on the condition of a few electrons per pulse. Two regions of constraint are indicated on figure 6 connected to two experimental conditions. An estimate of the NSMT1 to NSMT2 distance is included (vertical grey bar), as is the rise-time of the observations (graded horizontal bars). The overlap of these regions then indicates the most likely number of electrons per pulse after scaling the predicted SD by a factor of 4. This corresponds to the 95% confidence width of the distribution and better represents the maximal resolvable influence of the passing fs-e pulse.

Comparing our pressure gauge calibration with that of figures 5 and 6 allows deduction of an upper bound of 7 electrons per laser shot were arriving at the detector during collection of results. Although this measurement is somewhat rough, the fact that it provides an order of magnitude agreement with the ideal of a single electron per

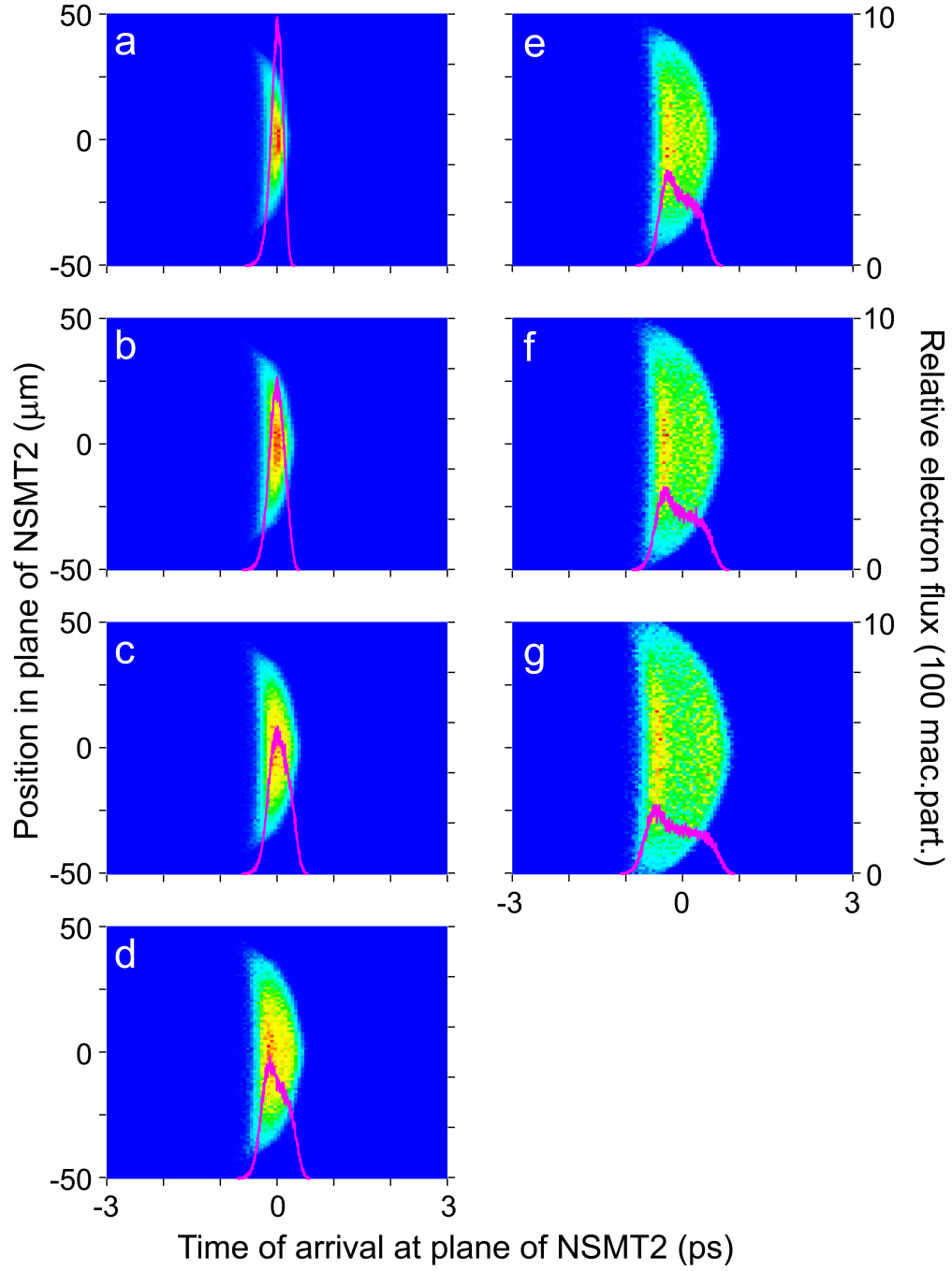


FIG. 7. Electron pulse spatial distribution as a function of arrival time at the plane of NSMT2 (colour density plots) and corresponding histogram of the relative electron flux (magenta line). The total charge of the electron pulse is varied from (a) 0e (No SC), (b) 1e, (c) 2e, (d) 3e, (e) 5e, (f) 7e and (g) 10e, with the total charge evenly distributed across the 50,000 GPT macro-particles used in the calculation. As the total charge of the pulse increases, a significant spatial and temporal spreading is found. The distribution best representing the results presented in figure 5 are (a), (b) and (c).

shot provides a strong indication that fs-ePPM is not only possible in the single electron regime, but capable of being performed with sufficient time resolution to resolve ultrafast surface dynamics. Looking carefully at figure 6, it is apparent that the femtosecond electron pulses employed in the present work are best described by an average total charge of approximately one electron per pulse. Such pulses are expected to be nearly free from space charge effects, and when coupled to DC or RF acceleration methods along with well-synchronized compression methods, will allow few-femtosecond or even attosecond duration pulses of electrons to be produced.

In figure 7 we show the predicted temporal and spatial distribution of our electron pulse in the plane of NSMT2 following the observations above. Increasing the total charge disperses the pulse in space and time while keeping the centre of charge at the same time, as anticipated. Figure 7(a-c) represent our best estimate of the distribution of our fs-e pulse at NSMT2. The influence of the geometric stretch is clear, causing a curved wavefront, and indicates how the manipulation of this wavefront would be beneficial to higher temporal resolution studies.

The simulation results show that the effect of space-charge is drastic, with a 3 electron bunch displaying a FWHM approximately twice that of a single electron bunch. The simulations predict that bunches of the order of 1-10 electron population remains relatively short, with a 10 electron bunch not exceeding 1 picosecond at the sample for the geometry investigated.

## VIII. CONCLUSIONS

Point projection electron microscopy of a tungsten nanotip has been performed with sub-micron scale spatial resolution using femtosecond laser emitted photoelectrons. By tuning the emission such that an average of a single electron is released per laser pulse, space-charge broadening is overcome allowing images with a temporal rise-time of around 500 fs associated with a standard deviation in time of around 120 fs to be obtained. This has been verified by tracking the propagation of charge along a tungsten nanotip induced by a femtosecond laser pulse using fs-ePPM with sub-micron scale spatial resolution and sub-picosecond temporal resolution. This is the first measurement of its kind to be performed on a tungsten NSMT and highlights the potential of femtosecond electron point-projection electron microscopy for extremely high resolution measurements of structural and charge dynamics in both space and time. The temporal resolution demonstrated here significantly expands the range of ultrafast processes that can be investigated with pulsed electron sources, particularly those susceptible to damage by transmission of keV to MeV pulses.

Simulations have been conducted to calculate the effects of space-charge on fs-e pulse length as a function of number of electrons per pulse for the specific field structure of the apparatus used. These simulations agree that the bunch lengths indicated by the results are realistic for the electron numbers believed to be present. The correlation between the timescales of the observed features and the best resolution predicted by the simulations strongly indicates that the single electron per laser shot emission regime is being exploited and that sub-100 fs temporal resolution is possible for probing electrons with sub-keV energies. We are investigating the ideal laser parameters for a range of fs-ePPM energies and anticipate a further increase in temporal resolution will be possible.

Installing a NSMT in a femtosecond electron microscopy or diffraction apparatus is straightforward, therefore the presented method could be adapted as a general fs-e pulse characterisation technique. This technique is best suited for low total charge electron pulses (less than hundreds of electrons) at repetition rates of tens of kilohertz and higher, rather than low (few kHz and lower) high charge ( $10^5$  electrons) systems.

## ACKNOWLEDGMENTS

These experiments were carried out with UFL1 from the Engineering and Physical Sciences Research Council (UK) Laser Loan Pool. We are very grateful to Dr. Ian Clark, Central Laser Facility, STFC Rutherford Appleton Laboratory (UK) for his support of this project during his management of the Laser Loan Pool. ARB acknowledges Postgraduate Studentship support from EPSRC, UK, and CWBM from a College of Science, Swansea University Postgraduate Research Studentship.

<sup>1</sup>P. Emma, R. Akre, J. Arthur, R. Bionta, C. Bostedt, J. Bozek, A. Brachmann, P. Bucksbaum, R. Coffee, F.-J. Decker, Y. Ding, D. Dowell, S. Edstrom, A. Fisher, J. Frisch, S. Gilevich, J. Hastings, G. Hays, P. Hering, Z. Huang, R. Iverson, H. Loos, M. Messerschmidt, A. Miahnahri, S. Moeller, H.-D. Nuhn, G. Pile, D. Ratner, J. Rzepiela, D. Schultz, T. Smith, P. Stefan, H. Tompkins, J. Turner, J. Welch, W. White, J. Wu, and G. Y. J. Galayda, “First lasing and operation of an angstrom-wavelength free-electron laser,” *Nat Photon* **4**, 641–647 (2010).

<sup>2</sup>E. Ruska, “The development of the electron microscope and of electron microscopy,” in *Nobel Lecture* (1986).

<sup>3</sup>B. J. Siwick, J. R. Dwyer, R. E. Jordan, and R. J. D. Miller, “An atomic-level view of melting using femtosecond electron diffraction,” *Science* **302**, 1382–1385 (2003), <http://www.sciencemag.org/content/302/5649/1382.full.pdf>.

<sup>4</sup>H. Ihee, J. Cao, and A. H. Zewail, “Ultrafast electron diffraction: structures in dissociation dynamics of  $\text{Fe}(\text{CO})_5$ ,” *Chemical Physics Letters* **281**, 10 – 19 (1997).

<sup>5</sup>H. N. Chapman, S. P. Hau-Riege, M. J. Bogan, S. Bajt, A. Barty, S. Boutet, S. Marchesini, M. Frank, B. W. Woods, W. H. Benner, R. A. London, U. Rohner, A. Szoke, E. Spiller, T. Moller, C. Bostedt, D. A. Shapiro, M. Kuhlmann, R. Treusch, E. Plonjes, F. Burmeister, M. Bergh, C. Caleman, G. Huldt, M. M. Seibert, and J. Hajdu, “Femtosecond time-delay x-ray holography,” *Nature* **448**, 676–679 (2007).

<sup>6</sup>R. P. Chatelain, V. R. Morrison, B. L. M. Klarenaar, and B. J. Siwick, “Coherent and incoherent electron-phonon coupling in graphite observed with radio-frequency compressed ultrafast electron diffraction,” *Phys. Rev. Lett.* **113**, 235502 (2014).

- <sup>7</sup>R. C. Dudek and P. M. Weber, “Ultrafast diffraction imaging of the electrocyclic ring-opening reaction of 1,3-cyclohexadiene,” *The Journal of Physical Chemistry A* **105**, 4167–4171 (2001), <http://dx.doi.org/10.1021/jp010122t>.
- <sup>8</sup>J. R. Dwyer, C. T. Hebeisen, R. Ernstorfer, M. Harb, V. B. Deyirmenjian, R. E. Jordan, and R. Dwayne Miller, “Femtosecond electron diffraction: ‘making the molecular movie’,” *Philosophical Transactions of the Royal Society of London A: Mathematical, Physical and Engineering Sciences* **364**, 741–778 (2006).
- <sup>9</sup>M. Gulde, S. Schweda, G. Storeck, M. Maiti, H. K. Yu, A. M. Wodtke, S. Schfer, and C. Ropers, “Ultrafast low-energy electron diffraction in transmission resolves polymer/graphene superstructure dynamics,” *Science* **345**, 200–204 (2014), <http://www.sciencemag.org/content/345/6193/200.full.pdf>.
- <sup>10</sup>A. A. Ishchenko, S. A. Aseyev, V. N. Bagratashvili, V. Y. Panchenko, and E. A. Ryabov, “Ultrafast electron diffraction and electron microscopy: present status and future prospects,” *Physics-Uspekhi* **57**, 633 (2014).
- <sup>11</sup>S. Lahme, C. Kealhofer, F. Krausz, and P. Baum, “Femtosecond single-electron diffraction,” *Structural Dynamics* **1**, 034303 (2014).
- <sup>12</sup>M. Ligges, C. Streubhr, T. Brazda, O. Posth, C. Hassel, G. Dumpich, P. Zhou, and D. von der Linde, “Observation of ultrafast lattice heating in thin metal films using time-resolved electron diffraction,” in *Symposium MM Ultrafast Processes in Materials Science*, MRS Proceedings, Vol. 1230 (2009).
- <sup>13</sup>R. Srinivasan, V. Lobastov, C.-Y. Ruan, and A. Zewail, “Ultrafast electron diffraction (ued),” *Helv. Chim. Acta* **86**, 1761–1799 (2003).
- <sup>14</sup>C. Ropers, D. R. Solli, C. P. Schulz, C. Lienau, and T. Elsaesser, “Localized multiphoton emission of femtosecond electron pulses from metal nanotips,” *Phys. Rev. Lett.* **98**, 043907 (2007).
- <sup>15</sup>B. Barwick, C. Corder, J. Strohaber, N. Chandler-Smith, C. Uiterwaal, and H. Batelaan, “Laser-induced ultrafast electron emission from a field emission tip,” *New Journal of Physics* **9**, 142 (2007).
- <sup>16</sup>C. Ropers, D. R. Solli, C. P. Schulz, C. Lienau, and T. Elsaesser, “Localized multiphoton emission of femtosecond electron pulses from metal nanotips,” *Phys. Rev. Lett.* **98**, 043907 (2007).
- <sup>17</sup>S. V. Yalunin, G. Herink, D. R. Solli, M. Krger, P. Hommelhoff, M. Diehn, A. Munk, and C. Ropers, “Field localization and rescattering in tip-enhanced photoemission,” *Annalen der Physik* **525**, L12–L18 (2013).
- <sup>18</sup>S. V. Yalunin, M. Gulde, and C. Ropers, “Strong-field photoemission from surfaces: Theoretical approaches,” *Phys. Rev. B* **84**, 195426 (2011).
- <sup>19</sup>G. Herink, D. R. Solli, M. Gulde, and C. Ropers, “Field-driven photoemission from nanostructures quenches the quiver motion,” *Nature* **483**, 190–193 (2012).
- <sup>20</sup>M. Schenk, M. Krüger, and P. Hommelhoff, “Strong-field above-threshold photoemission from sharp metal tips,” *Phys. Rev. Lett.* **105**, 257601 (2010).
- <sup>21</sup>P. Hommelhoff, C. Kealhofer, and M. A. Kasevich, “Ultrafast electron pulses from a tungsten tip triggered by low-power femtosecond laser pulses,” *Phys. Rev. Lett.* **97**, 247402 (2006).
- <sup>22</sup>P. Hommelhoff, Y. Sortais, A. Aghajani-Talesh, and M. A. Kasevich, “Field emission tip as a nanometer source of free electron femtosecond pulses,” *Phys. Rev. Lett.* **96**, 077401 (2006).
- <sup>23</sup>M. Kruger, M. Schenk, M. Forster, and P. Hommelhoff, “Attosecond physics in photoemission from a metal nanotip,” *J. Phys. B: At., Mol. Opt. Phys.* **45**, 074006 (2012).
- <sup>24</sup>M. Muller, A. Paarmann, and R. Ernstorfer, “Femtosecond electrons probing currents and atomic structure in nanomaterials,” *Nat Commun* **5**, – (2014).
- <sup>25</sup>L. Waldecker, R. Berton, and R. Ernstorfer, “Compact femtosecond electron diffractometer with 100 keV electron bunches approaching the single-electron pulse duration limit,” *Journal of Applied Physics* **117**, 044903 (2015).
- <sup>26</sup>P. Baum, “Towards ultimate temporal and spatial resolutions with ultrafast single-electron diffraction,” *Journal of Physics B: Atomic, Molecular and Optical Physics* **47**, 124005 (2014).
- <sup>27</sup>P. Baum, “Towards ultimate temporal and spatial resolutions with ultrafast single-electron diffraction,” *Journal of Physics B: Atomic, Molecular and Optical Physics* **47**, 124005 (2014).
- <sup>28</sup>J.-N. Longchamp, T. Latychevskaia, C. Escher, and H.-W. Fink, “Graphene unit cell imaging by holographic coherent diffraction,” *Phys. Rev. Lett.* **110**, 255501 (2013).
- <sup>29</sup>J.-N. Longchamp, T. Latychevskaia, C. Escher, and H.-W. Fink, “Low-energy electron transmission imaging of clusters on free-standing graphene,” *Applied Physics Letters* **101**, 113117 (2012).
- <sup>30</sup>F. Smann, M. F. Kling, and P. Hommelhoff, “From attosecond control of electrons at nano-objects to laser-driven electron accelerators,” in *Attosecond Nanophysics* (Wiley-VCH Verlag GmbH, 2014) pp. 155–196.
- <sup>31</sup>A. Schiffrin, T. Paasch-Colberg, and M. Schultze, “Controlling and tracking electric currents with light,” in *Attosecond Nanophysics* (Wiley-VCH Verlag GmbH, 2014) pp. 235–280.
- <sup>32</sup>C. Lienau, M. Raschke, and C. Ropers, “Ultrafast nano-focusing for imaging and spectroscopy with electrons and light,” in *Attosecond Nanophysics* (Wiley-VCH Verlag GmbH, 2014) pp. 281–324.
- <sup>33</sup>S. H. Chew, K. Pearce, C. Spth, A. Guggenmos, J. Schmidt, F. Smann, M. F. Kling, U. Kleineberg, E. Mrsell, C. L. Arnold, E. Lorek, P. Rudawski, C. Guo, M. Miranda, F. Ardana, J. Mauritsson, A. L’Huillier, and A. Mikkelsen, “Imaging localized surface plasmons by femtosecond to attosecond time-resolved photoelectron emission microscopy,” in *Attosecond Nanophysics* (Wiley-VCH Verlag GmbH, 2014) pp. 325–364.
- <sup>34</sup>A. R. Bainbridge and W. A. Bryan, “Velocity map imaging of femtosecond laser induced photoelectron emission from metal nanotips,” *New Journal of Physics* **16**, 103031 (2014).
- <sup>35</sup>T. L. Gilton, J. P. Cowin, G. D. Kubiak, and A. V. Hamza, “Intense surface photoemission: Space charge effects and self-acceleration,” *Journal of Applied Physics* **68**, 4802–4810 (1990).
- <sup>36</sup>S. Passlack, S. Mathias, O. Andreyev, D. Mittnacht, M. Aeschlimann, and M. Bauer, “Space charge effects in photoemission with a low repetition, high intensity femtosecond laser source,” *Journal of Applied Physics* **100**, 024912 (2006).
- <sup>37</sup>J. Hoffrogge, J. Paul Stein, M. Krger, M. Frster, J. Hammer, D. Ehberger, P. Baum, and P. Hommelhoff, “Tip-based source of femtosecond electron pulses at 30 keV,” *Journal of Applied Physics* **115**, 094506 (2014), <http://dx.doi.org/10.1063/1.4867185>.
- <sup>38</sup>T. van Oudheusden, P. L. E. M. Pasmans, S. B. van der Geer, M. J. de Loos, M. J. van der Wiel, and O. J. Luiten, “Compression of subrelativistic space-charge-dominated electron bunches for single-shot femtosecond electron diffraction,” *Phys. Rev. Lett.* **105**, 264801 (2010).
- <sup>39</sup>O. J. Luiten, T. V. Oudheusden, B. Siwick, E. D. Jong, W. O. t. Root, and B. V. d. Geer, “Extreme beams for single-shot ultrafast electron diffraction,” *Microscopy and Microanalysis* **14**, 494–495 (2008).

- <sup>40</sup>V. S. Yakovlev, M. I. Stockman, F. Krausz, and P. Baum, “Atomic-scale diffractive imaging of sub-cycle electron dynamics in condensed matter,” *Scientific Reports* **5**, 14581 EP – (2015), article.
- <sup>41</sup>E. Quinonez, J. Handali, and B. Barwick, “Femtosecond photoelectron point projection microscope,” *Review of Scientific Instruments* **84**, 103710 (2013).
- <sup>42</sup>H. Yanagisawa, C. Hafner, P. Doná, M. Klöckner, D. Leuenberger, T. Greber, M. Hengsberger, and J. Osterwalder, “Optical control of field-emission sites by femtosecond laser pulses,” *Phys. Rev. Lett.* **103**, 257603 (2009).
- <sup>43</sup>H. Yanagisawa, C. Hafner, P. Doná, M. Klöckner, D. Leuenberger, T. Greber, J. Osterwalder, and M. Hengsberger, “Laser-induced field emission from a tungsten tip: Optical control of emission sites and the emission process,” *Phys. Rev. B* **81**, 115429 (2010).
- <sup>44</sup>M. Hada, K. Pichugin, and G. Sciaini, “Ultrafast structural dynamics with table top femtosecond hard x-ray and electron diffraction setups,” *The European Physical Journal Special Topics* **222**, 1093–1123 (2013).